Band structures extending to very high spin in ^{126}Xe

C. Rønn Hansen, G. Sletten,* G. B. Hagemann, B. Herskind, and D. R. Jensen
Niels Bohr Institute, Blegdamsvej 17, DK-2100 Copenhagen, Denmark and GANIL, BP 55027, F-14076 Caen Cedex 5, France

P. Bringel, C. Engelhardt, H. Hübel, A. Neußer-Neffgen, and A. K. Singh
Helmholtz-Institut für Strahlen- und Kernphysik, Universität Bonn, Nußallee 14–16, D-53115 Bonn, Germany

M. P. Carpenter, R. V. F. Janssens, T. L. Khoo, and T. Lauritsen
Physics Division, Argonne National Laboratory, Argonne, IL 60439, USA

P. Bednarczyk, T. Byrski, and D. Curien
IPHC-DRS, ULP, CNRS, IN2P3, B. P. 28, F-67037 Strasbourg, France

G. Benzoni, A. Bracco, F. Camera, and S. Leoni
Dipartemento di Fisica and INFN, Sezione di Milano, I-20133 Milano, Italy

R. M. Clark and P. Fallon
Lawrence Berkeley National Laboratory, Ca 94720 Berkeley, USA

A. Korichi and J. Roccaz
CSNSM, F-91406 Orsay, F-91406 Orsay Cedex, France.

A. Maj
Niewodniczanski Institute of Nuclear Physics, ul. Radzikowskiego 152, 31-342 Krakow, Poland

J. N. Wilson
IPN Orsay, F-91406 Orsay Cedex, France

J. C. Lisle
University of Manchester, Shuster Laboratory, Brunswick str. Manchester M13 9PL, United Kingdom

T. Steinhardt and O. Thelen
Institut für Kernphysik, Universität zu Köln, D-50937 Köln, Germany

S. W. Ødegård
Department of Physics, University of Oslo, PB 1048 Blindern, N-0316 Oslo, Norway
(Received 12 April 2007; published 11 September 2007)

High-spin states in ^{126}Xe have been populated in the ^{82}Se(^{48}Ca,4n)^{126}Xe reaction in two experiments, one at the VIVITRON accelerator in Strasbourg using the Euroball detector array, and a subsequent one with ATLAS at Argonne using the Gammasphere Ge-detector array. Levels and assignments made previously for ^{126}Xe up to $I = 20$ have been confirmed and extended. Four regular bands extending to a spin of almost $I = 60$, which are interpreted as two pairs of signature partners with opposite parity, are identified for the first time. The $\alpha = 0$ partner of each pair is connected to the lower-lying levels, whereas the two $\alpha = 1$ partners remain floating. A fractional Doppler shift analysis of transitions in the strongest populated $(\pi, \alpha) = (-, 0)$ band provides a value of $5.2^{0.4}_{0.5}$ b for the transition quadrupole moment, which can be related to a minimum in the potential-energy surface calculated by the ULTIMATE CRANKER cranked shell-model code at $\epsilon \approx 0.35$ and $\gamma \approx 5^\circ$. The four lowest bands calculated for this minimum compare well with the two signature pairs experimentally observed over a wide spin range. A sharp upbend at $\hbar\omega \sim 1170$ keV is interpreted as a crossing with a band involving the $j_{15/2}$ neutron orbital, for which pairing correlations are expected to be totally quenched. The four long bands extend to within ∼5 spin units of a crossing with an yrast line defined by calculated hyperdeformed transitions and will serve as important stepping stones into the spin region beyond $60\hbar$ for future experiments.

DOI: 10.1103/PhysRevC.76.034311 PACS number(s): 23.20.Lv, 23.20.En, 27.60.+j, 29.30.−h

I. INTRODUCTION

Nuclei in the $A = 120$–130 mass region are considered transitional with regard to their shape at low and high angular

*sletten@nbi.dk

momentum. The rotational motion leads to Coriolis-induced alignment effects, which in the present case are governed by the $h_{11/2}$ unique parity intruder subshell for both neutrons and protons. A most conspicuous feature of these nuclei is their γ softness at low and moderate spin and the large susceptibility to polarization effects from the excitation of individual quasiprotons and quasineutrons. The alignment of the protons tends to drive the nuclear shape toward prolate deformation, whereas the alignment of neutrons induces an oblate shape. Already the presence of a single $h_{11/2}$ neutron will drive the nucleus toward oblate deformation, whereas additional neutrons have only a small effect [1].

Seiffert *et al.* [2] have established 13 band structures in ^{126}Xe up to a spin of about 20$\hbar$ based on experiments with the ^{116}Cd(^{13}C,3n) and ^{123}Te(α,n) reactions. Firm assignments of spin and parity to the majority of the levels were made on the basis of angular distribution and linear polarization measurements of the γ rays and comparison of level properties to calculations within the O(6) limit of the interacting boson model and the cranked shell model [2].

Theoretical calculations show that at higher angular momentum a stable minimum in the potential energy surface, representing a well deformed prolate shape develops. A tendency toward non-axial symmetry of these nuclei at extreme spins and high excitaion, the socalled Jacobi transition region, gives rise to a substantially smaller fission width than expected for prolate nuclei [3]. Therefore, they provide an opportunity for populating levels at extreme spins. A hyperdeformed (HD) minimum at $I \geqslant 70$ is predicted in ^{126}Xe by liquid drop model calculations [4] with a fission barrier of several MeV at the highest spins. Similarly, a deep prolate minimum and a high barrier against fission at $\epsilon_2 \approx 0.95$ is found in calculations with the ULTIMATE CRANKER (UC) code [5]. These predictions have been the motivation for the two major experimental campaigns reported in this work. Separate accounts of the efforts to indentify ridges in the coincidence matrices corresponding to hyperdeformation in ^{126}Xe are presented in Refs. [6,7]. Ridges are formed by cascading transitions when the energy of these increase regularly with spin, and the distance between ridges reflects the moment of inertia of the spinning nucleus. We note at this point that a large number of rotationally damped transitions contribute to the ridges and therefore increase the chances for measuring the moment of inertia of a spinning nucleus. In fact, the first discovery of superdeformation in ^{152}Dy was by a ridge analysis [8] 2 years before the substantiation of this by discrete line measurements [9]. In the present article, we shall describe the discrete-line spectroscopy that takes advantage of the assignments previously given in Ref. [2] and extends the spectroscopy considerably. An outstanding feature of the level structure is the remarkable regularity, which appears beyond spin 20, where four newly identified bands extend almost to spin 60 at more than 42 MeV of excitation.

II. EXPERIMENTAL DETAILS

Two experiments, both with the reaction ^{82}Se(^{48}Ca, xn)$^{130-x}$Xe have been performed using major Ge-detector arrays. The first experiment, hereafter referred to as Xe1, was carried out at the VIVITRON at Strasbourg where $1.9{\cdot}10^9$ events were detected by the Euroball array [10] with the Ge-fold selection $\mathrm{Ge_{sup}} \geqslant 3$. The incident beam energy was 195 MeV, entering through the Au backing of the Se target, and was reduced to about 190 MeV at mid-target. The beam intensity was less than 1pnA. The second experiment, hereafter referred to as Xe2, was performed at the ATLAS accelerator at Argonne National Laboratory (ANL) and γ-ray coincidences were measured with the Gammasphere array [11]. The beam energy was 205 MeV incident on the target and about 200 MeV at midtarget. A total of 2.8×10^9 events with a fold selection $\mathrm{Ge_{sup}} \geqslant 5$ was recorded. In both experiments the γ-ray coincidence events were stored on magnetic tape.

Selenium is a chemical homolog of sulfur and is far from an ideal target for heavy-ion bombardment. Self-supporting foils for use with heavy-ion beams cannot be produced and for supported films, the tendency for sublimation and melting, even at about 200°C, requires special care. The targets with a thickness of 500 μg/cm^2 were produced by evaporation of 98.8% enriched ^{82}Se onto a 500-μg/cm^2 Au foil and by finally evaporating an 80-μg/cm^2 Au protecting layer onto the Se. These targets could successfully withstand beam intensities up to about 1 pnA used in the Xe1 experiment. In the Xe2 experiment, however, where up to 4 pnA were used, the beam was slightly defocussed and wobbled over the target which was mounted on four quadrants of a rotating wheel [12]. In this way a low heat deposit per unit area in the target was achieved. At the same time a continous monitoring of the target was possible via an online spectrum of the trigger rate versus the coordinates of the target surface as a function of time. These targets remained undamaged after 7 days of ^{48}Ca bombardment, most of the time at an intensity of 4 pnA.

III. ANALYSIS AND RESULTS

The γ-ray coincidence events from both experiments were sorted into databases on disk from which cubes and four-dimentional hypercubes were produced using the Radware software package [13]. A main difference between the Xe1 and the Xe2 data set is the parameters from the bismuth germanate (BGO) calorimeter that provide a tool to identify high multiplicity events, independently of the Ge-fold selection. The data from Xe1 were used to build the level scheme shown in Figs. 1 and 2 and to exploit gating with the BGO ball for extreme multiplicity cascades, possibly originating from hyperdeformed states. The Xe2 data set was taken more than 2 years later, this time without a calorimeter, but with a strongly increased Ge-fold restriction and an increased magnitude of high Ge-fold events in the data set. The more extensive Xe2 data were therefore used primarily to search for γ-rays originating from hyperdeformed states using the detailed information at high spin from the Xe1 data set. This search was unsuccessful, but the improved quality and magnitude of the data set became essential for extracting angular distributions, to disentangle difficult coincidence relationships

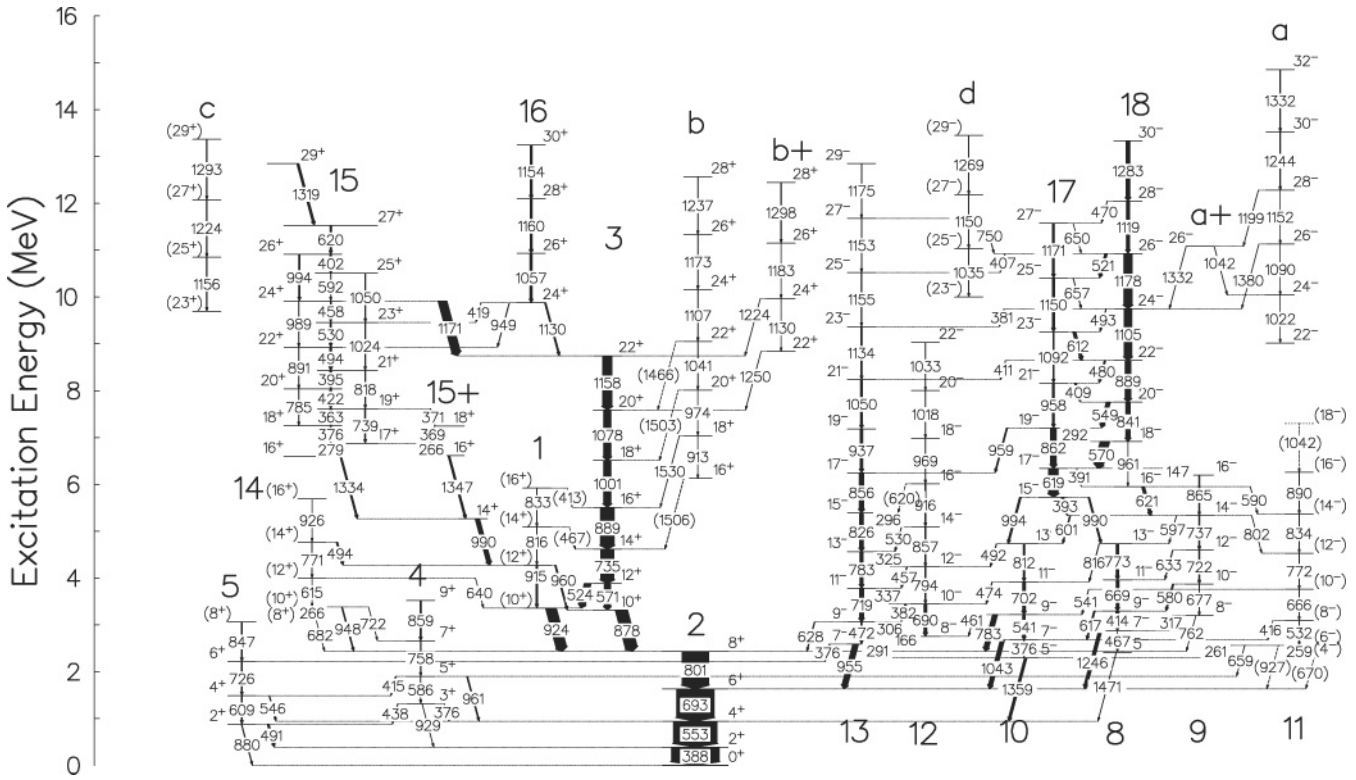

FIG. 1. Partial, low-spin level scheme of ^{126}Xe. The labeling used in Ref. [2] for the previously known bands is maintained, bands 16, 17, 18, **a**, **b**, **c**, and **d** are new structures identified in the present work. The widths of the arrows correspond to intensity, whereas transitions with less than about 20% of the 388.3 keV ground-state transition are drawn as arrows with a standard width.

and to determine the transition quadrupole moment in the strongest high spin band. For the angular distributions, gated matrices of γ rays were built, using a combination of detectors at forward and backward angles (43 crystals), against the events from angles around 90° (50 crystals) taken from the Xe2 database.

The experimental data are presented in Tables I and II. Table I contain the level energies, the spin and parity assignments, the transition energies, the γ-ray intensities, the angular intensity ratios, the extracted multipole order and the $B(M1)/B(E2)$ ratios for selected cases. The R_Θ ratios given in the tables were created from two asymmetric coincidence matrices. One matrix was created with a gate list including all detectors on one axis and the detectors in the angular interval $17° \leqslant \Theta \leqslant 50°$ and $130° \leqslant \Theta \leqslant 163°$ on the other axis. The second matrix was sorted with the same gate list including all detectors on one axis and the detectors in the angular interval $70° \leqslant \Theta \leqslant 130°$ on the other axis. The ratios R_Θ were obtained from the intensities of the peaks,

$$R_\Theta = \frac{I_{(\text{forwd.}-\text{backwd.})}}{I_{\sim 90°}}.$$

This procedure has the advantage of higher statistical accuracy compared to directional correlation from oriented states (DCO) ratios. For stretched quadrupole radiation $R_\Theta = 1.40 \pm 0.04$, whereas for stretched dipoles $R_\Theta = 0.74 \pm 0.02$ is expected. These values are based on experimental results for transitions with multipole order determined in the work of Granderath *et al.* [1] and Seiffert *et al.* [2]. We note that values of R_Θ= 1.40 and 0.7 may alternatively correspond to mixed $M1/E2$ (or $M2/E1$) $\Delta I = 0$ transitions or a $\Delta I = 1$ quadrupole transition, respectively. These latter possibilities are less likely because unstretched transitions are usually less competitive due to smaller energy than the streched ones, if available.

The newly observed long bands extending from the spin 20 region to very high spins are named **a**, **b**, **c**, and **d**. Table II contains the experimental results for these bands. The numbering of the bands used in Ref. [2] is maintained and extended with bands 16, 17, and 18. The structure of ^{126}Xe as it appears in light- and heavy-ion induced reactions changes dramatically in the spin range around 20$\hbar$, and the level scheme is, therefore, shown in two parts for clarity. Figure 1 shows the low-spin part of the levels, and Fig. 2 contains the levels of the higher spin range. In both figures a guide to the intensity flow is given by the widths of the transition arrows, but for details we refer to Tables I and II. In the tables all intensities are given relative to the 388 keV $2^+ \rightarrow 0^+$ ground-state transition. Spins and parities are determined from the angular distribution of connecting transitions. If given in parenthesis, they are less certain, deduced from systematics or comparison to model predictions. In many cases, however, interwoven band structures lock mutual values.

TABLE I. Level energies, spin, and parity assignments, γ-ray energy, relative intensities, angular distribution ratios R_Θ (see Sec. III), assigment of multipole order and $B(M1)/B(E2)$ ratios of transitions in bands 1–18. With very few exceptions, all transitions above $15\hbar$ are newly observed in this work. For bands 15, 16, 17, and 18 all transitions are new observations. The intensities are measured relative to the 388.3 keV $2^+ \rightarrow 0^+$ ground-state transition. Closely lying and weak transitions are fitted separately, whereas the intensities of the stronger lines are fitted with routines of the RADWARE programme package [13]. In some cases the R_Θ value is not given due to overlap of transitions with similar energy, preventing a meaningful assignment of the multipole order.

Band ID	Level energy (keV)	$I_i^\pi \rightarrow I_f^\pi$	E_γ (keV)	Intensity	R_θ	$E(\lambda)$ $M(\lambda)$	$B(M1)/B(E2)$ (μ_N^2/e^2b^2)
Ground	388.3	$2^+ \rightarrow 0^+$	388.3	1000	1.17 ± 0.01	$E2$	
band	941.3	$4^+ \rightarrow 2^+$	553.0	926.6 ± 29.3	1.27 ± 0.02	$E2$	
2	1634.1	$6^+ \rightarrow 4^+$	692.8	798.0 ± 25.0	1.33 ± 0.02	$E2$	
	2434.7	$8^+ \rightarrow 6^+$	800.7	567.6 ± 18.2	1.39 ± 0.04	$E2$	
1	3359.0	$10^+ \rightarrow 8^+$	924.2	223.5 ± 7.9	1.39 ± 0.04	$E2$	
	4272.2	$12^+ \rightarrow 10^+$	915.1	29.9 ± 2.8	1.41 ± 0.04	$E2$	
		$12^+ \rightarrow 10^+$	960.1	25.8 ± 2.5	1.42 ± 0.07	$E2$	
	5088.0	$14^+ \rightarrow 12^+$	816.3	7.2 ± 1.3	1.39 ± 0.10	$E2$	
		$14^+ \rightarrow 14^+$	(466.9)	<0.2			
	5920.8	$16^+ \rightarrow 14^+$	832.8	4.3 ± 4.0	1.42 ± 0.12	$E2$	
		$16^+ \rightarrow 16^+$	(413.2)	<0.4			
3	3312.9	$10^+ \rightarrow 8^+$	878.3	254.7 ± 9.1	1.39 ± 0.04	$E2$	
	3883.5	$12^+ \rightarrow 10^+$	524.4	139.8 ± 5.7			
		$12^+ \rightarrow 10^+$	570.6	136.9 ± 5.8	1.42 ± 0.04	$E2$	
	4618.5	$14^+ \rightarrow 12^+$	734.8	277.3 ± 9.4	1.45 ± 0.06	$E2$	
	5507.6	$16^+ \rightarrow 14^+$	889.1	290.7 ± 10.2	1.42 ± 0.04	$E2$	
	6508.3	$18^+ \rightarrow 16^+$	1000.7	161.3 ± 5.7	1.38 ± 0.05	$E2$	
	7585.9	$20^+ \rightarrow 18^+$	1077.6	153.9 ± 5.6	1.37 ± 0.05	$E2$	
	8744.3	$22^+ \rightarrow 20^+$	1158.5	197.5 ± 7.2	1.39 ± 0.09	$E2$	
	9915.1	$24^+ \rightarrow 22^+$	1170.8	184.3 ± 12.6	1.40 ± 0.13	$E2$	
8	2412.8	$5^- \rightarrow 4^+$	1471.5	2.8 ± 1.3	0.87 ± 0.20	$E1$	
	2879.8	$7^- \rightarrow 6^+$	1245.9	68.5 ± 4.2	0.90 ± 0.20	$E1$	
		$7^- \rightarrow 5^-$	467.0	3.0 ± 1.0			
	3293.7	$9^- \rightarrow 7^-$	414.0	65.9 ± 3.0	1.37 ± 0.12	$E2$	
		$9^- \rightarrow 7^-$	617.1	28.9 ± 2.2			
	3962.4	$11^- \rightarrow 9^-$	669.0	60.5 ± 5.6	1.35 ± 0.12	$E2$	
	4734.9	$13^- \rightarrow 11^-$	773.0	51.1 ± 4.0	1.41 ± 0.10	$E2$	
		$13^- \rightarrow 11^-$	816.1	6.2 ± 1.7			
9	3196.6	$8^- \rightarrow 7^-$	316.9	4.8 ± 1.1			
		$8^- \rightarrow 8^+$	762.1	<0.5			
	3873.4	$10^- \rightarrow 9^-$	580.0	27.8 ± 3.4			2.0 ± 0.3
		$10^- \rightarrow 8^-$	677.0	7.2 ± 0.9			
	4595.2	$12^- \rightarrow 10^-$	721.7	22.3 ± 2.1			
		$12^- \rightarrow 11^-$	632.8	9.6 ± 1.9			0.23 ± 0.05
	5331.9	$14^- \rightarrow 12^-$	737.0	23.3 ± 4.0			
		$14^- \rightarrow 12^-$	600.8	20.2 ± 1.9			
		$14^- \rightarrow 13^-$	596.7	3.0 ± 1.2			0.71 ± 0.15
		$14^- \rightarrow 12^-$	801.7	0.8 ± 0.4			
	6198.1	$16^- \rightarrow 14^-$	865.0	14.4 ± 4.4			
10	2299.6	$5^- \rightarrow 4^+$	1358.7	51.6 ± 5.9			
	2676.9	$7^- \rightarrow 6^+$	1042.8	87.4 ± 5.6			
		$7^- \rightarrow 5^-$	376.5	8.2 ± 1.3			
	3217.5	$9^- \rightarrow 8^+$	783.1	104.0 ± 6.0			
		$9^- \rightarrow 7^-$	540.6	54.0 ± 3.4			
		$9^- \rightarrow 8^-$	460.7	3.0 ± 0.8			0.018 ± 0.005
	3919.4	$11^- \rightarrow 9^-$	702.1	59.9 ± 4.5			
		$11^- \rightarrow 10^-$	474.2	8.0 ± 0.9			0.15 ± 0.02
	4731.1	$13^- \rightarrow 11^-$	811.8	36.5 ± 2.6			
		$13^- \rightarrow 12^-$	492.3	9.1 ± 1.3			0.51 ± 0.08

TABLE I. *(Continued.)*

Band ID	Level energy (keV)	$I_i^\pi \rightarrow I_f^\pi$	E_γ (keV)	Intensity	R_θ	$E(\lambda)$ $M(\lambda)$	$B(M1)/B(E2)$ (μ_N^2/e^2b^2)
11	2303.4	$(4^-) \rightarrow 6^+$	(670.3)	<0.1			
	2561.3	$(6^-) \rightarrow 5^-$	261.0	2.7 ± 0.3			0.12 ± 0.08
		$(6^-) \rightarrow 5^+$	658.8	2.1 ± 0.3			
		$(6^-) \rightarrow 4^-$	259.9	1.0 ± 0.6			
		$(6^-) \rightarrow 6^+$	(927.1)	<0.1			
	3092.9	$(8^-) \rightarrow (6^-)$	531.7	5.2 ± 2.1			–
		$(8^-) \rightarrow 7^-$	416.2	<0.1			
	3758.8	$(10^-) \rightarrow 9^-$	541.2	5.9 ± 2.3			0.8 ± 0.5
		$(10^-) \rightarrow (8^-)$	666.1	4.5 ± 2.4			
	4530.3	$(12^-) \rightarrow (10^-)$	772.0	4.1 ± 0.7			
	5363.8	$(14^-) \rightarrow (12^-)$	833.7	2.9 ± 0.8			
	6255.2	$(16^-) \rightarrow (14^-)$	890.3	5.7 ± 2.5			
	(7297.5)	$(18^-) \rightarrow (16^-)$	(1042.3)	<0.3			
12	2755.9	$8^- \rightarrow 7^-$	166.4	69.7 ± 2.3		$E1$	
	3444.5	$10^- \rightarrow 8^-$	690.1	59.6 ± 2.5		$E2$	
		$10^- \rightarrow 9^-$	382.2	39.4 ± 1.6			1.29 ± 0.08
	4238.5	$12^- \rightarrow 10^-$	793.9	18.4 ± 1.4	1.39 ± 0.08	$E2$	
		$12^- \rightarrow 11^-$	456.6	14.3 ± 1.1			1.8 ± 0.2
	5095.2	$14^- \rightarrow 12^-$	857.4	16.5 ± 3.0	1.40 ± 0.10	$E2$	
		$14^- \rightarrow 13^-$	530.0	5.4 ± 0.8			0.71 ± 0.17
	6011.4	$16^- \rightarrow 14^-$	916.0	14.4 ± 0.2	1.39 ± 0.12	$E2$	
		$16^- \rightarrow 15^-$	(620.0)	<0.3			0.04 ± 0.42
	6981.0	$18^- \rightarrow 16^-$	969.0	10.2 ± 1.9	1.40 ± 0.13	$E2$	
	8000.1	$20^- \rightarrow 18^-$	1018.5	7.7 ± 2.4	1.39 ± 0.14	$E2$	
	9033.2	$22^- \rightarrow 20^-$	1033.1	<1.0	1.40 ± 0.23	$E2$	
13	2589.3	$7^- \rightarrow 6^+$	954.8	117.4 ± 5.8	0.97 ± 0.03	$E1$	
		$7^- \rightarrow 6^+$	376.0	12.5 ± 1.0		$E1$	
		$7^- \rightarrow 5^-$	291.3	5.7 ± 0.8			
	3062.2	$9^- \rightarrow 8^-$	306.1	71.0 ± 2.2			1.43 ± 0.10
		$9^- \rightarrow 7^-$	472.4	28.3 ± 1.8		$E2$	
		$9^- \rightarrow 8^+$	628.4	12.2 ± 2.1		$E1$	
	3781.3	$11^- \rightarrow 9^-$	718.7	87.0 ± 3.2		$E2$	
		$11^- \rightarrow 10^-$	337.3	14.9 ± 0.8			0.59 ± 0.04
	4564.7	$13^- \rightarrow 11^-$	783.2	65.7 ± 3.2	1.36 ± 0.05	$E2$	
		$13^- \rightarrow 12^-$	325.2	4.3 ± 0.8			0.39 ± 0.07
	5391.0	$15^- \rightarrow 13^-$	826.2	82.0 ± 3.3	1.37 ± 0.05	$E2$	0.20 ± 0.07
		$15^- \rightarrow 14^-$	296.1	1.6 ± 0.6			0.20 ± 0.07
	6246.9	$17^- \rightarrow 15^-$	856.0	99.8 ± 4.6	1.39 ± 0.06	$E2$	
	7183.7	$19^- \rightarrow 17^-$	936.8	59.0 ± 2.7	1.37 ± 0.07	$E2$	
	8233.8	$21^- \rightarrow 19^-$	1050.1	42.5 ± 2.2	1.41 ± 0.07	$E2$	
	9368.0	$23^- \rightarrow 21^-$	1134.3	23.9 ± 1.7	1.42 ± 0.10	$E2$	
	10522.9	$(25^-) \rightarrow (23^-)$	1155.3	11.1 ± 2.3	1.39 ± 0.13	$E2$	
	11676.7	$27^- \rightarrow 25^-$	1153.0	8.4 ± 5.0	1.39 ± 0.13	$E2$	
		$27^- \rightarrow 26^-$	749.8	5.3 ± 2.2		$(M1)$	2.1 ± 1.5
	12850.9	$29^- \rightarrow 27^-$	1175.8	5.4 ± 4.1	1.40 ± 0.17	$E2$	
15	6597.4	$16^+ \rightarrow 14^+$	1333.7	32.8 ± 4.0	1.39 ± 0.10	$E2$	
	6876.8	$17^+ \rightarrow 16^+$	279.4	30.5 ± 1.2	0.75 ± 0.05	$(M1)$	
		$17^+ \rightarrow 16^+$	265.7	13.0 ± 0.7	0.71 ± 0.04	$(M1)$	
	7252.7	$18^+ \rightarrow 17^+$	375.8	29.6 ± 1.4	0.73 ± 0.05	$(M1)$	
	7615.4	$19^+ \rightarrow 18^+$	362.6	46.1 ± 1.7	0.73 ± 0.04	$(M1)$	9.0 ± 0.7
		$19^+ \rightarrow 17^+$	739.4	18.2 ± 1.2	1.40 ± 0.09	$E2$	
		$19^+ \rightarrow 18^+$	370.9	6.4 ± 0.5	0.75 ± 0.05	$(M1)$	
	8037.8	$20^+ \rightarrow 19^+$	422.4	39.6 ± 1.5	0.73 ± 0.05	$(M1)$	14.9 ± 1.4
		$20^+ \rightarrow 18^+$	785.0	7.3 ± 0.6		$E2$	

TABLE I. *(Continued.)*

Band ID	Level energy (keV)	$I_i^\pi \rightarrow I_f^\pi$	E_γ (keV)	Intensity	R_θ	$E(\lambda)$ $M(\lambda)$	$B(M1)/B(E2)$ (μ_N^2/e^2b^2)
	8432.8	$21^+ \rightarrow 20^+$	394.9	42.8 ± 1.6	0.73 ± 0.04	$(M1)$	10.9 ± 1.3
		$21^+ \rightarrow 19^+$	817.8	16.1 ± 1.7	1.41 ± 0.16	$E2$	
	8926.7	$22^+ \rightarrow 21^+$	493.8	44.4 ± 1.8	0.75 ± 0.05	$(M1)$	21.0 ± 3.4
		$22^+ \rightarrow 20^+$	890.7	6.8 ± 1.1		$E2$	
	9457.2	$23^+ \rightarrow 22^+$	530.5	26.6 ± 1.2	0.78 ± 0.08	$(M1)$	10.6 ± 1.1
		$23^+ \rightarrow 21^+$	1023.6	13.1 ± 1.2	1.38 ± 0.16	$E2$	
	9915.6	$24^+ \rightarrow 23^+$	458.4	18.0 ± 1.0	0.68 ± 0.15	$(M1)$	19.4 ± 3.2
		$24^+ \rightarrow 22^+$	989.3	6.3 ± 1.0		$E2$	
	10507.9	$25^+ \rightarrow 23^+$	1050.4	15.6 ± 1.5	1.40 ± 0.16		
		$25^+ \rightarrow 24^+$	592.0	6.1 ± 2.6		$(M1)$	1.7 ± 0.7
	10910.2	$26^+ \rightarrow 25^+$	402.3	37.7 ± 1.7	0.76 ± 0.09	$(M1)$	
		$26^+ \rightarrow 24^+$	993.0	22.3 ± 2.4	1.38 ± 0.18	$E2$	
		$26^+ \rightarrow 24^+$	993.8	4.5 ± 1.3		$E2$	
	11530.5	$27^+ \rightarrow 26^+$	620.4	34.0 ± 4.6	0.85 ± 0.07	–	
15+	5264.0	$14^+ \rightarrow 12^+$	990.3	90.6 ± 4.9	1.42 ± 0.9	$E2$	
	6611.0	$16^+ \rightarrow 14^+$	1347.0	37.7 ± 3.8	1.42 ± 0.18	$E2$	
	7245.0	$18^+ \rightarrow 17^+$	369.0	4.8 ± 0.9	0.75 ± 0.05	$(M1)$	
16	9876.0	$24^+ \rightarrow 22^{)}$	1130.3	28.3 ± 1.4	1.40 ± 0.12	$E2$	
		$24^+ \rightarrow 23^+$	418.6	7.5 ± 0.7	0.75 ± 0.08	$(M1)$	
		$24^+ \rightarrow 22^+$	949.3	6.9 ± 1.2	1.44 ± 0.18	$E2$	
	10933.0	$26^+ \rightarrow 24^+$	1057.0	48.0 ± 3.2	1.38 ± 0.09	$E2$	
	12093.2	$28^+ \rightarrow 26^+$	1160.2	46.3 ± 3.7	1.41 ± 0.10	$E2$	
	13247.3	$30^+ \rightarrow 28^+$	1154.2	42.1 ± 2.9	1.41 ± 0	$E2$	
17	5724.8	$15^- \rightarrow 14^-$	393.1	48.3 ± 2.4	0.92 ± 0.07	$(M1)$	
		$15^- \rightarrow 13^-$	993.7	35.4 ± 2.0	1.41 ± 0.17	$E2$	
		$15^- \rightarrow 13^-$	989.9	30.5 ± 2.0	1.38 ± 0.18	$E2$	
	6344.0	$17^- \rightarrow 15^-$	619.2	205.1 ± 8.0	1.39 ± 0.05		
		$17^- \rightarrow 16^-$	391.0	1.4 ± 1.7		$(M1)$	0.007 ± 0.008
	7205.9	$19^- \rightarrow 17^-$	862.0	122.8 ± 4.8	1.42 ± 0.07		
		$19^- \rightarrow 18^-$	292.0	36.27 ± 1.6	0.94 ± 0.08	$(M1)$	3.4 ± 0.2
		$19^- \rightarrow 17^-$	958.6	23.7 ± 2.1	1.40 ± 0.20	$E2$	
	8164.0	$21^- \rightarrow 19^-$	958.1	41.8 ± 3.0	1.39 ± 0.15	$E2$	
		$21^- \rightarrow 20^-$	409.0	36.3 ± 1.7	0.98 ± 0.10	$(M1)$	7.1 ± 0.6
	9256.2	$23^- \rightarrow 22^-$	612.1	63.2 ± 3.2		$(M1)$	11.8 ± 1.3
		$23^- \rightarrow 21^-$	1092.3	25.1 ± 2.4	1.43 ± 0.21	$E2$	
	10406.3	$25^- \rightarrow 23^-$	1150.2	45.2 ± 3.0	1.43 ± 0.19	$E2$	
		$(25^-) \rightarrow (24^-)$	657.1	5.9 ± 1.6		$(M1)$	0.65 ± 0.18
	11577.2	$27^- \rightarrow 25^-$	1171.0	40.1 ± 2.9	1.42 ± 0.17	$E2$	
		$27^- \rightarrow 26^-$	650.0	<0.3		$(M1)$	
18	5953.0	$16^- \rightarrow 14^-$	621.1	60.5 ± 5.4			
		$16^- \rightarrow 14^-$	589.6	2.4 ± 0.5			
	6913.9	$18^- \rightarrow 17^-$	570.0	194.4 ± 7.2	0.71 ± 0.02	$(M1)$	
		$18^- \rightarrow 16^-$	960.6	<0.3		$E2$	
	7755.0	$20^- \rightarrow 18^-$	841.1	95.3 ± 4.2	1.41 ± 0.08	$E2$	
		$20^- \rightarrow 19$	549.1	85.8 ± 3.5	0.69 ± 0.02	$(M1)$	1.59 ± 0.10
	8644.2	$22^- \rightarrow 20^-$	889.2	127.7 ± 5.6	1.40 ± 0.07	$E2$	
		$22^- \rightarrow 21^-$	480.1	30.1 ± 1.5	0.95 ± 0.08	$(M1)$	0.82 ± 0.07
	9749.1	$24^- \rightarrow 22^-$	1104.9	165.3 ± 5.9	1.38 ± 0.06	$E2$	
		$24^- \rightarrow 23^-$	492.8	7.9 ± 1.9		$(M1)$	1.2 ± 0.3
		$24^- \rightarrow 23^-$	381.4	6.9 ± 1.2	0.72 ± 0.05	$(M1)$	
	10927.3	$26^- \rightarrow 24^-$	1178.3	175.5 ± 6.0	1.40 ± 0.07	$E2$	
		$26^- \rightarrow 25^-$	521.0	51.8 ± 2.5		$(M1)$	3.5 ± 0.2
		$26^- \rightarrow 25^-$	407.0	2.0 ± 0.8			
	12046	$28^- \rightarrow 26^-$	1119.0	63.7 ± 3.1	1.42 ± 0.12	$E2$	
		$28^- \rightarrow 27^-$	469.5	5.5 ± 1.1		$(M1)$	3.5 ± 0.2
	13330.6	$30^- \rightarrow 28^-$	1283.4	87.2 ± 4.0	1.39 ± 0.13	$E2$	

TABLE II. Level energies, spin, and parity assignments, γ-ray energies, relative intensities, angular distribution ratios R_Θ (see Sec. III), and assigment of multipole order of transitions in bands **a**–**d**. All transitions are newly observed in this work. The intensities are measured relative to the 388.3-keV $2^+ \rightarrow 0^+$ ground-state transition. Closely lying and weak transitions are fitted separately, whereas the intensities of the stronger lines are fitted with routines of the RADWARE program package [13]. In some cases the R_Θ value is not given due to overlap of transitions with similar energy, preventing a meaningful assignment of the multipole order. Bands **a** and **b** are connected. Bands **c** and **d** are not connected to lower-lying structures by known transitions. Level energies are indicated by the sum of Y or X and the transition energies of the two bands, respectively.

Band ID	Level energy (keV)	$I_i^\pi \rightarrow I_f^\pi$	E_γ (keV)	Intensity	R_θ	$E(\lambda)$ $M(\lambda)$
a	10039.6	$24^- \rightarrow 22^-$	1022.0	1.8 ± 1.4	1.32 ± 0.19	$(E2)$
	11129.8	$26^- \rightarrow (24^-)$	1090.4	1.3 ± 1.0	1.39 ± 0.17	$E2$
		$26^- \rightarrow 24^-$	1378.7	1.0 ± 1.9	1.58 ± 0.45	$E2$
	12277.0	$26^- \rightarrow 24^-$	1152.2	3.5 ± 0.1	1.41 ± 0.12	$E2$
		$28^- \rightarrow 26^-$	1198.7	1.8 ± 0.6	1.42 ± 0.22	$E2$
	13521.4	$30^- \rightarrow 28^-$	1244.4	13.2 ± 1.9	1.41 ± 0.08	$E2$
	14853.4	$32^- \rightarrow 30^-$	1332.1	13.0 ± 1.0	1.41 ± 0.08	$E2$
	16284.8	$34^- \rightarrow 32^-$	1431.5	12.4 ± 1.3	1.44 ± 0.09	$E2$
	17825.5	$36^- \rightarrow 34^-$	1540.7	9.6 ± 1.0	1.42 ± 0.12	$E2$
	19483.7	$38^- \rightarrow 36^-$	1658.2	8.5 ± 1.2	1.44 ± 0.13	$E2$
	21264.8	$40^- \rightarrow 38^-$	1781.3	7.6 ± 1.1	1.42 ± 0.15	$E2$
	23172.1	$42^- \rightarrow 40^-$	1907.4	6.3 ± 1.0	1.41 ± 0.15	$E2$
	25208.9	$44^- \rightarrow 42^-$	2036.8	5.1 ± 0.9	1.40 ± 0.20	$E2$
	27372.4	$46^- \rightarrow 44^-$	2163.6	4.5 ± 0.8	1.37 ± 0.29	$E2$
	29656.2	$48^- \rightarrow 46^-$	2283.8	3.3 ± 0.5	1.40 ± 0.33	$E2$
	32008.1	$50^- \rightarrow 48^-$	2354.0	1.3 ± 0.3	1.50 ± 0.46	$E2$
	34355.0	$52^- \rightarrow 50^-$	2349.0	0.8 ± 0.3	(1.50 ± 0.46)	$(E2)$
	36797.0	$54^- \rightarrow 52^-$	2442.0	0.7 ± 0.2		$(E2)$
	39312.0	$56^- \rightarrow 54^-$	2515.0	0.4 ± 0.1		$(E2)$
a+	11079.5	$26^- \rightarrow 24^-$	1042	2.2 ± 0.5	(0.72 ± 0.13)	$(E2)$
		$26^- \rightarrow 24^-$	1332.2	2.0 ± 1.1	(1.40 ± 0.18)	$(E2)$
a$\sim$	32077.0	$50^- \rightarrow 48^-$	2421.0	0.3 ± 0.5		
	34527.0	$52^- \rightarrow 50^-$	2450.0	0.8 ± 0.4		
b	6126.0	$16^+ \rightarrow 14^+$	(1505.7)	3.7 ± 2.0		
	7039.0	$18^+ \rightarrow 16^+$	913.0	2.0 ± 1.2	1.40 ± 0.20	$E2$
	8010.5	$20^+ \rightarrow 18^+$	974.0	3.0 ± 1.5	1.40 ± 0.13	$E2$
		$20^+ \rightarrow 18^+$	(1503.3)	<1.0		
	9051.3	$22^+ \rightarrow 20^+$	1040.9	4.0 ± 0.5	1.39 ± 0.10	$E2$
		$22^+ \rightarrow 20^+$	(1466.3)	<0.2		
	10158.1	$24^+ \rightarrow 22^+$	1106.8	9.8 ± 3.0	1.38 ± 0.10	$E2$
	11331.5	$26^+ \rightarrow 24^+$	1173.4	8.9 ± 3.2	1.41 ± 0.13	$E2$
	12568.5	$28^+ \rightarrow 26^+$	1237.1	5.7 ± 2.3	1.39 ± 0.17	$E2$
	13887.2	$30^+ \rightarrow 28^+$	1318.7	4.3 ± 2.4	1.40 ± 0.19	$E2$
	15255.7	$32^+ \rightarrow 30^+$	1368.8	3.6 ± 0.7	1.40 ± 0.19	$E2$
		$32^+ \rightarrow 30^+$	1403.0	2.8 ± 1.0	1.40 ± 0.29	E2
	16727.9	$34^+ \rightarrow 32^+$	1472.2	7.7 ± 2.2	1.39 ± 0.13	$E2$
	18293.1	$36^+ \rightarrow 34^+$	1565.3	7.3 ± 2.7	1.40 ± 0.14	$E2$
	19954.6	$38^+ \rightarrow 36^+$	1661.5	7.0 ± 1.9	1.39 ± 0.16	$E2$
	21711.1	$40^+ \rightarrow 38^+$	1756.6	5.1 ± 1.8	1.39 ± 0.17	$E2$
	23563.2	$42^+ \rightarrow 40^+$	1852.1	4.4 ± 1.6	1.41 ± 0.18	$E2$
	25510.3	$44^+ \rightarrow 42^+$	1947.5	3.9 ± 1.5	1.38 ± 0.19	$E2$
	27552.1	$46^+ \rightarrow 44^+$	2041.9	2.7 ± 1.2	1.40 ± 0.23	$E2$
	29689.9	$48^+ \rightarrow 46^+$	2137.8	2.5 ± 1.1	1.43 ± 0.25	$E2$
	31920.9	$50^+ \rightarrow 48^+$	2231.0	2.1 ± 0.9	1.43 ± 0.26	$E2$
	34238.0	$52^+ \rightarrow 50^+$	2317.1	1.8 ± 0.6	1.43 ± 0.29	$E2$
	36593.3	$54^+ \rightarrow 52^+$	2360.9	1.2 ± 0.7	1.42 ± 0.32	$E2$
	38923.9	$56^+ \rightarrow 54^+$	2336.2	0.5 ± 0.6	1.40 ± 0.37	$E2$

TABLE II. *(Continued.)*

Band ID	Level energy (keV)	$I_i^\pi \rightarrow I_f^\pi$	E_γ (keV)	Intensity	R_θ	$E(\lambda)$ $M(\lambda)$
b+	8836.2	$22^+ \rightarrow 20^+$	1250.1	1.1 ± 2.1	1.43 ± 0.23	$E2$
	9967.0	$24^+ \rightarrow 22^+$	1130.5	3.0 ± 1.5	1.38 ± 0.24	$E2$
		$24^+ \rightarrow 22^+$	1224.1	0.9 ± 1.7		$E2$
	11149.0	$26^+ \rightarrow 24^+$	1183.2	4.0 ± 2.5	1.40 ± 0.25	$E2$
	12445.4	$28^+ \rightarrow 26^+$	1297.5	9.0 ± 2.2	1.40 ± 0.26	$E2$
	13854.1	$30^+ \rightarrow 28^+$	1409.9	7.5 ± 1.6	1.38 ± 0.29	$E2$
		$30^+ \rightarrow 28^+$	1285.8	<0.4		$E2$
c	$Y + 1156.4$	$(25^+) \rightarrow (23^+)$	1156.4	0.8 ± 1.2		$(E2)$
	$Y + 2380.6$	$(27^+) \rightarrow (25^+)$	1224.2	2.3 ± 2.1	1.38 ± 0.17	$E2$
	$Y + 3673.3$	$(29^+) \rightarrow (27^+)$	1292.7	3.3 ± 1.0	1.40 ± 0.15	$E2$
	$Y + 5043.4$	$(31^+) \rightarrow (29^+)$	1370.1	5.0 ± 2.0	1.40 ± 0.13	$E2$
	$Y + 6488.3$	$(33^+) \rightarrow (31^+)$	1444.9	4.7 ± 2.0	1.39 ± 0.13	$E2$
	$Y + 8014.1$	$(35^+) \rightarrow (33^+)$	1526.1	4.0 ± 1.9	1.38 ± 0.14	$E2$
	$Y + 9624.0$	$(37^+) \rightarrow (35^+)$	1609.6	3.1 ± 1.8	1.39 ± 0.15	$E2$
	$Y + 11320.8$	$(39^+) \rightarrow (37^+)$	1696.8	1.9 ± 1.7	1.43 ± 0.15	$E2$
	$Y + 13107.5$	$(41^+) \rightarrow (39^+)$	1786.7	2.0 ± 1.6	1.39 ± 0.16	$E2$
	$Y + 14984.7$	$(43^+) \rightarrow (41^+)$	1877.2	1.8 ± 1.3	1.42 ± 0.16	$E2$
	$Y + 16953.2$	$(45^+) \rightarrow (43^+)$	1968.5	1.3 ± 1.3	1.39 ± 0.20	$E2$
	$Y + 19004.0$	$(47^+) \rightarrow (45^+)$	2050.8	1.3 ± 1.2	1.42 ± 0.25	$E2$
	$Y + 21097.0$	$(49^+) \rightarrow (47^+)$	2093.0	1.0 ± 1.0	1.44 ± 0.32	$E2$
	$Y + 23226.4$	$(51^+) \rightarrow (49^+)$	2129.4	0.8 ± 1.0	1.44 ± 0.32	$E2$
	$Y + 25413.8$	$(53^+) \rightarrow (51^+)$	2187.4	0.6 ± 1.4		$(E2)$
	$Y + 27673.5$	$(55^+) \rightarrow (53^+)$	2259.7	0.4 ± 1.0		$(E2)$
	$Y + 30018.0$	$(57^+) \rightarrow (55^+)$	2344.5	0.3 ± 0.6		$(E2)$
	$Y + (32345.7)$	$(59^+) \rightarrow (57^+)$	(2327.7)	<0.1		$(E2)$
d	$X + 1034.7$	$(25^-) \rightarrow (23^-)$	1034.7	6.2 ± 2.1	1.39 ± 0.17	$E2$
	$X + 2184.2$	$(27^-) \rightarrow (25^-)$	1149.5	7.3 ± 3.9	1.42 ± 0.16	$E2$
	$X + 3453.0$	$(29^-) \rightarrow (27^-)$	1268.8	6.3 ± 2.9	1.37 ± 0.16	$E2$
	$X + 4839.6$	$(31^-) \rightarrow (29^-)$	1386.6	4.8 ± 1.6	1.39 ± 0.17	$E2$
	$X + 6341.8$	$(33^-) \rightarrow (31^-)$	1502.2	4.4 ± 1.5	1.38 ± 0.18	$E2$
	$X + 7944.7$	$(35^-) \rightarrow (33^-)$	1602.9	4.1 ± 1.3	1.43 ± 0.20	$E2$
	$X + 9654.2$	$(37^-) \rightarrow (35^-)$	1709.5	1.2 ± 1.1	1.41 ± 0.22	$E2$
	$X + 11477.5$	$(39^-) \rightarrow (37^-)$	1823.3	1.1 ± 1.1	1.43 ± 0.21	$E2$
	$X + 13417.1$	$(41^-) \rightarrow (39^-)$	1939.6	1.0 ± 1.3	1.42 ± 0.23	$E2$
	$X + 15466.8$	$(43^-) \rightarrow (41^-)$	2049.8	1.0 ± 1.3	1.44 ± 0.32	$E2$
	$X + 17616.9$	$(45^-) \rightarrow (43^-)$	2150.0	0.9 ± 1.0	1.41 ± 0.35	$E2$
	$X + 19853.7$	$(47^-) \rightarrow (45^-)$	2236.8	0.6 ± 0.8	1.45 ± 0.44	$E2$
	$X + 22174.5$	$(49^-) \rightarrow (47^-)$	2320.8	0.3 ± 0.5	1.40 ± 0.25	$E2$
	$(X + 24598.9)$	$(51^-) \rightarrow (49^-)$	(2424.4)	<0.1		$(E2)$

A. Positive-parity bands

The ground-state band, in Ref. [2] also referred to as band 2, terminates at an 8^+ level at 2434.7 keV, where it connects to band 1, which has a $\pi(h_{11/2})^2$ structure and to band 3 that has a $\nu(h_{11/2})^2$ structure [1]. The present work extends band 3 by only one transition to $I = 24$ and identifies two transitions connecting the two different $(h_{11/2})^2$ structures, bands 1 and 3, at the spin 14 and 16 levels. Bands 4 and 5, which are of vibrational nature, and lie quite high in energy above the yrast line, are only weakly populated in the ^{82}Se(^{48}Ca,xn) reaction. Similarly, bands 6 and 7 reported in Ref. [2] are not observed in the present work, probably also due to their off-yrast nature. Band 14 is observed but not extended to higher spin in this work. It is shown in Fig. 1 with the assignments given in Ref. [2]. Band 15, not connected to the ground-state levels in Ref. [2], is observed to spin and parity 27^+ in the present work, and two decay routes connecting it to the ground state are identified. One of these proceeds via levels of a structure labeled 15+ in Fig. 1, which might possibly correspond to low-lying members of a high-K band. The $E2$ character of the 990-, 1334-, and 1347-keV transitions extracted from the data gives positive parity and firm spin assignments to bands 15 and 15+. A strong $E2$ transition of 1319 keV populates the 27^+ level of band 15, but no further structures connected to it could be identified with certainty. Band 16 is newly observed in this work. It decays by an $E2$ transition into the $I^\pi = 22^+$ level of band 3 and extends by three $E2$ transitions to an $I^\pi = 30^+$ state, but no further transitions to

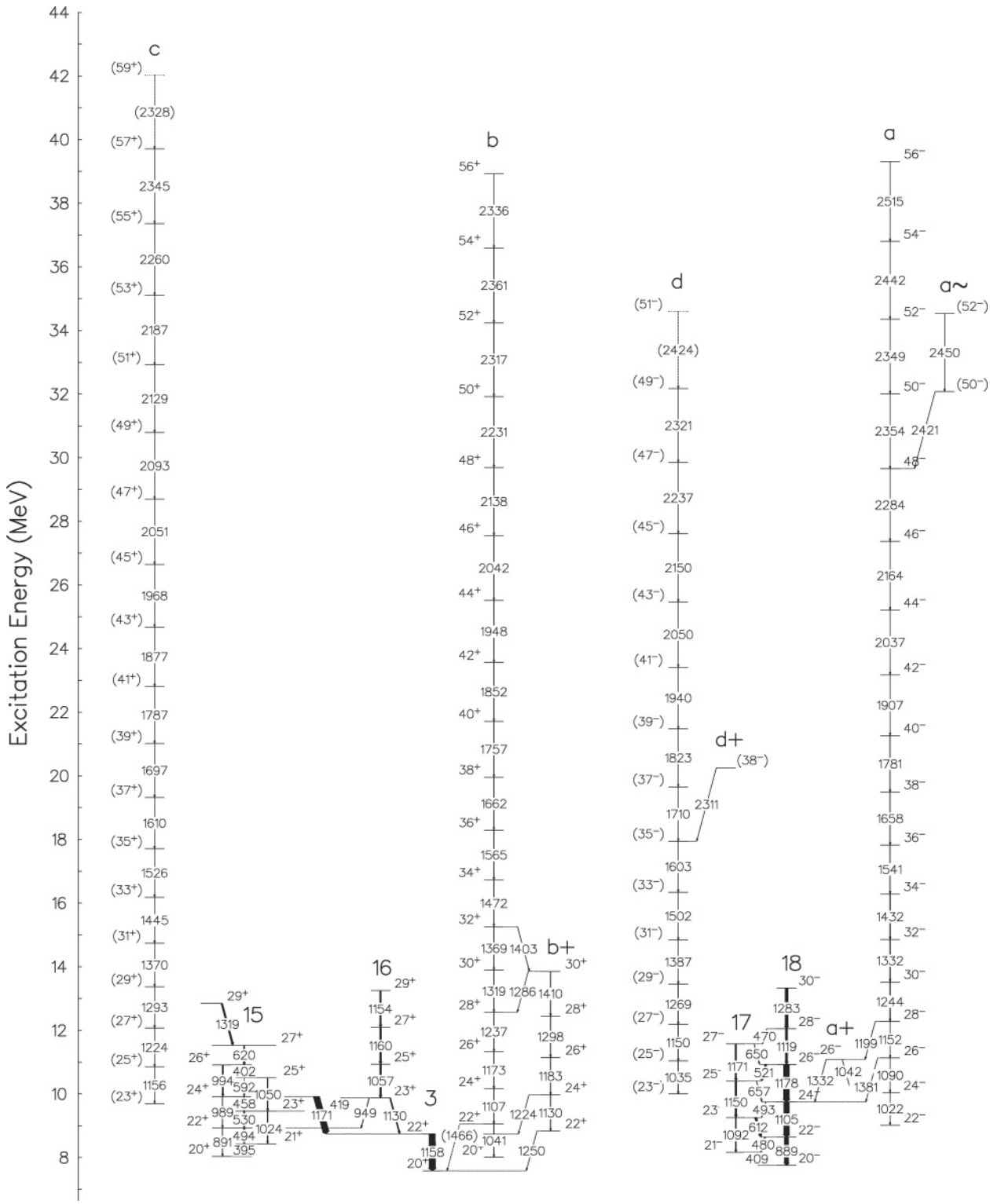

FIG. 2. Partial, high-spin level scheme of ^{126}Xe. The newly identified collective structures are labeled **a**, **b**, **c**, and **d**, whereas previously reported levels [2] are labeled 3 and 15. New levels and transitions have been added to band 15, whereas bands 16, 17, and 18 are new.

higher energies or any signature partner to band 16 could be found.

The newly identified band **b** connects to the $\nu(h_{11/2})^2$ structure of band 3 at the $I = 14$ and 16 levels, as shown in Fig. 1 and extends to $I = 56$ at an excitation energy of 38.9 MeV as indicated in Fig. 2. The double-gated spectrum on clean transitions beyond $I = 30$, presented in Fig. 3, documents the coincidence relationships of band **b** and its forking structure $\mathbf{b}^+$. The 1250-keV quadrupole transition determines $I = 22$ for the bottom level of band $\mathbf{b}^+$, and the

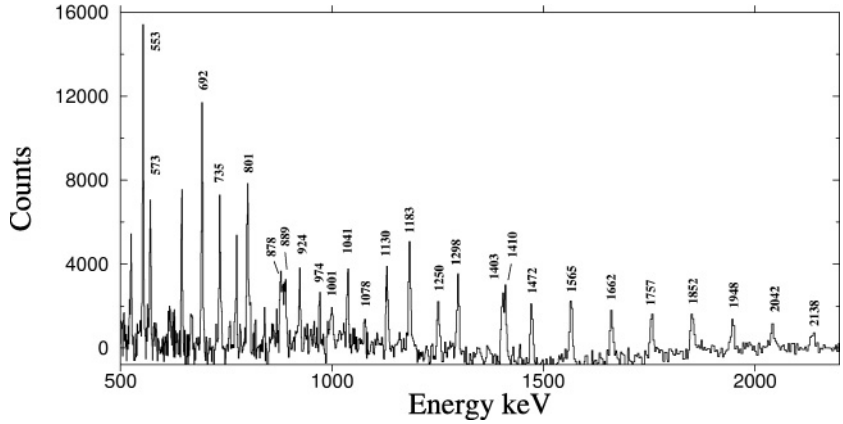

FIG. 3. Double-gated spectrum of band **b** illustrating the decay into band 3 and eventually the ground-state band. The spectrum was created with two gate-lists containing transitions at [1757, 1662, 1565, 1472] and [1403, 1410, 1298, 1183] keV, respectively. The strong unmarked γ rays below 800 keV are known transitions in the neighboring nucleus ^{125}Xe. The reduced intensity of the peaks in the 1100- to 1800-keV region is due to the eight gates imposed in this energy interval.

1403- and 1286-keV $E2$ transitions feeding and depopulating the $I = 30^+$ level of band $\mathbf{b}^+$ firmly connect the two bands. Both bands have parity and signature $(\pi, \alpha) = (+, 0)$ and they interact at $I^\pi = 30^+$.

Although not connected to the low-lying bands by firm evidence, the placement of band **c** shown in Figs. 1 and 2 is the most probable considering transition energies and intensities in the band. The intensities are evaluated on the basis of the relative intensities of the four long bands as described in Sec. III C of this chapter. It decays to $\pi = +$ structures as **b** does and the suggested assignment as the (+,1) partner of band **b** therefore agrees with this placement. This will be discussed further in Sec. IV. The decay of band **c** into lower lying structures involves the 29^+ level feeding band 15 via a 1319-keV transition, but no definite decay route could be established.

B. Negative-parity bands

Ten different negative-parity bands are observed in the present work, two of them extending to spins beyond 50. The lowest lying of the negative-parity bands are band 8 and its most probable signature partner, band 9. In Ref. [2] evidence is given for an $I^\pi = 3^-$ bandhead. In the present work, however, most of the in-band intensity is drained at $I^\pi = 7^-$ by a 1245-keV transition to the 8^+ level of the ground-state band. Only a weak decay is seen to the 5^- state, but no connection to the 3^- level is identified. Similarly, the low-lying levels of band 9 reported in Ref. [2] are not observed. The 8^- state at 3196.6 keV decays into the $I^\pi = 7^-$ level of band 8 and with a very weak branch to the 8^+ state of the ground band. The failure to observe the low-lying transitions in bands 8 and 9 can be explained by a different side-feeding to the low-lying states of these bands in the ^{82}Se(^{48}Ca,xn) reaction.

Bands 10 and 11 are presumably also signature partners with a structure very similar to bands 8 and 9. A 802-keV transition from band 9 into the $I = 12$ level of band 11 and weak transitions from band 11 into band 10 at the spin 8 and 6 levels supports this suggestion. The spin and parity assignments of band 10 are firm and the (−,0) assignment of band 11 is, therefore, the most probable. All four structures are populated by the two newly observed bands 17 and 18, which most likely are higher-seniority quasiparticle bands and which we identify as signature partners with $(\pi, \alpha) = (-, 1)$ and (−,0), respectively. A fourth pair of negative-parity signature partners is bands 12 and 13. The 955-keV $E1$ transition to the 6^+ state of the ground band confirms the 7^- assignment of the 2589.3-keV level of band 13. A 750-keV transition connects the 27^- level of band 13 to the 26^- state of band 18 and provides a further check on the assignments.

Two of the newly observed long bands, extending beyond spin 50, presumably have negative parity and are shown as bands **a** and **d** in Fig. 2. Their features and assignments will be discussed in Sec. IV.

The connection of band **a** to the lower-lying structures is illustrated by the spectrum presented in Fig. 4. The band

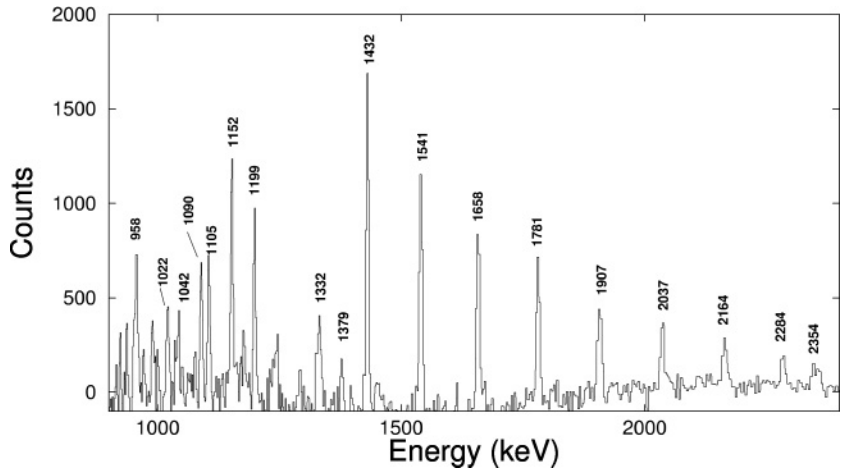

FIG. 4. Double-gated spectrum of band **a** illustrating the decay into bands 17 and 18 via the intermediate **a**+ level. The 1332-keV transition is in self-coincidence. The appearence of a weak 1178-keV peak might suggest a placement of level **a**+ two spin units higher than shown and band **a** lifted 1178 keV in energy, see text.

connects to band 18, which has a parity and signature assignment of (−,0), through an isolated level at 11 MeV with $I^\pi = 26^-$ by a 1332-keV $E2$ transition. The 26^- level decays also back into band **a**, presumably due to mixing of the two 26^- states. Parity and signature of the two bands are, therefore, the same. The lowest state of band **a** has spin 22^- at 9 MeV and the band extends by 17 consecutive $E2$ transitions to $I^\pi = 56^-$ at 39 MeV.

The placement of band **a** shown in Fig. 2 could in principle be lifted by two units of spin. The appearance of the 1178-keV transition, visible in the spectrum shown in Fig. 4, could indicate that the 1332-keV transition from the $I^\pi = 26^-$ level labeled $\mathbf{a}^+$ could populate band 18 at its $I = 26^-$ level at 10927.3 keV and not the $I^\pi = 24^-$ state, which is 1178 keV lower in energy. Because there are transitions of similar energy elsewhere in the ^{126}Xe level scheme and in the neighboring isotopes, the placement based on triple and quadruple coincidences alone has some uncertainty. We will come back to this question in the discussion of Sec. IV, using arguments from derived quantities.

C. Population of the highest-spin states

The population of band **a** is the highest among the bands extending beyond spin $I = 50$ and the intensity of the $30 \rightarrow 28$, 1244 keV transition of this band is 1.3% of the ground-state transition. The relative intensities of bands **a** to **d** have been estimated from spectra created with a sum of six double gates in each of the four bands placed on either side of a transition of about 1600 keV. Relative to band **a**, the strengths of bands **b**, **c**, and **d** are 0.9, 0.6, and 0.4, respectively, in the spin range 32–44.

As shown in Figs. 1 and 2, the bands numbered 15–18 are not identified to spins higher than about $30\hbar$ in the present work. This does not mean that there are no coincident transitions preceeding those drawn in the figures. One example is the precursors of the assigned $30^+ \rightarrow 28^+$, 1283-keV transition of band 18. Among these precursors we find a relatively strong γ ray of 2545 keV and a number of weaker ones in the energy range from 1500 to 1800 keV. None of these feeding transitions could be placed into a regular band structure and one might surmise that band 18 as well as some of the other bands terminate at about spin 30.

D. Transition quadrupole moment of band a

The recoiling Xe ions require about 100 fs to penetrate the 500-μg/cm^2 Se target, which implies that γ rays from highly excited, rapidly rotating deformed nuclei will be emitted during their passage through the target. Even though this target is thin, the velocity v/c of the recoiling nuclei varies by about 6% from one end to the other and this variation is sufficient for measurements of fractional Doppler shifts, F_τ, for the fastest transitions, as demonstrated in Refs. [14,15].

The fractional shifts were determined from the experimental recoil velocities relative to the velocity calculated from the kinematics of the reaction, here defined as the velocity at midtarget. Estimates of the velocity which the ^{126}Xe-recoil had at the emission of a given transition in band **a** were determined from the dependence of the observed peak widths to the value of v/c applied in the correction for Doppler shifts. A minimum peak-width corresponds to the average v/c for a particular transition. Gated spectra were produced at 13 different values of v/c. The full width at half maximum (FWHM) for the peaks were obtained from fits using RADWARE programs [13]. Figure 5, upper left panel, shows a minimum at $v/c = 0.0344$ for the 1540 keV $I = 36 \rightarrow 34$ transition. The upper right

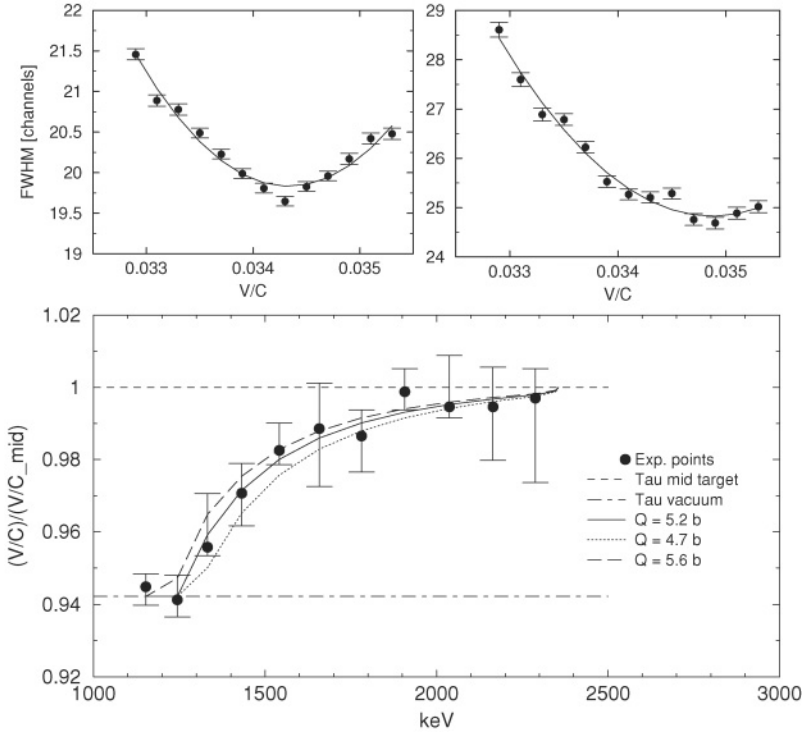

FIG. 5. Peak width analysis of the 1540 keV $36^- \rightarrow 34^-$ and the 1907 keV $42^- \rightarrow 40^-$ transition in band **a** shown in the left and the right upper panels, respectively. The lower panel presents the fractional Doppler shifts for 11 transitions of band **a** based on the minimum FWHM extracted from graphs of the type shown above, as a function of the transition energy. Curves calculated for three different values of the transition quadrupole moment are compared and the value $Q_t = 5.2$ b is adopted.

panel of Fig. 5 shows a minimum at a larger v/c for the 1907 keV $I = 42 \rightarrow 40$ transition, emitted three steps earlier in the cascade. In this way the minimum FWHM was determined for 11 transitions and the corresponding v/c values in the energy range from 1100 to 2300 keV were normalized to the v/c value at the middle of the target as shown in the lower panel of Fig. 5. A simple rotational model assuming the reduced $E2$ transition probability

$$B(E2, I \rightarrow I-2) = \frac{5}{16\pi}(e\hat{Q}_2)^2 \frac{2I-3}{2I+1}, \qquad (1)$$

where $\hat{Q}_2 \propto \epsilon \cos(\gamma + 30^\circ)$ in the high-spin limit, was used together with tabulated stopping powers [16]. Here $\hat{Q}_2$ refers to the rotation axis as quantization axis and relates to the usual Q_o for axial symmetry and quantization along the symmetry axis as $Q_o = \sqrt{\frac{8}{3}}\hat{Q}_2$ [17]. Fits to the F_τ values with the quadrupole moment $Q_t = \sqrt{\frac{8}{3}}\hat{Q}_2$ as a free parameter for the average quadrupole moment of the band was performed as shown in Fig. 5, lower panel. The best fit to the experimental values is obtained for $Q_t = 5.2^{+0.4}_{-0.5}$ b. Curves for $Q_t = 4.7$ and 5.6 b are also shown, indicating the sensitivity of the method. The adopted value corresponds to an axis ratio of $\sim$1.3 for an axially symmetric deformed Xe nucleus.

IV. DISCUSSION OF THE LONG HIGH-SPIN BANDS

The four long collective bands, **a**, **b**, **c**, and **d**, newly identified in the present work, extend into the spin region near $I = 60$. At this limit, even the structures close to yrast have intensities below the detection sensitivity of the Gammasphere array for discrete-line spectroscopy in ^{126}Xe. In the following we will discuss the properties of these four bands, relating the transition quadrupole moments of band **a**, the positions in the energy-spin plane, the dynamic moments of inertia, and the evolution of alignment to theoretical calculations with the UC code [5]. As the present data do not add decisive new information to the low-spin part of the level scheme, we will not repeat comments on the earlier configuration assignments [1,2].

First, we want to make some general comments on the level scheme related to the long bands. There are missing links in the level structure shown in Fig. 1 and Fig. 2; only band **b** is firmly linked to the low-lying structures. The strongest populated band, band **a**, is linked as shown in Fig. 1 with very high certainty but due to the many energy degeneracies of the γ-ray energies, as mentioned in Sec. III B, this band could possibly be lifted up by two spin units and 1178 keV in energy. Figure 6 shows the level energies of bands **a** and **b**, with a rigid rotor reference subtracted, as a function of spin.

For band **a** the two placements discussed here are shown. In the lower panel, the band is placed as shown in Fig. 1, whereas the upper panel presents the band lifted by two spin units and 1178 keV in excitation energy. The higher spin and

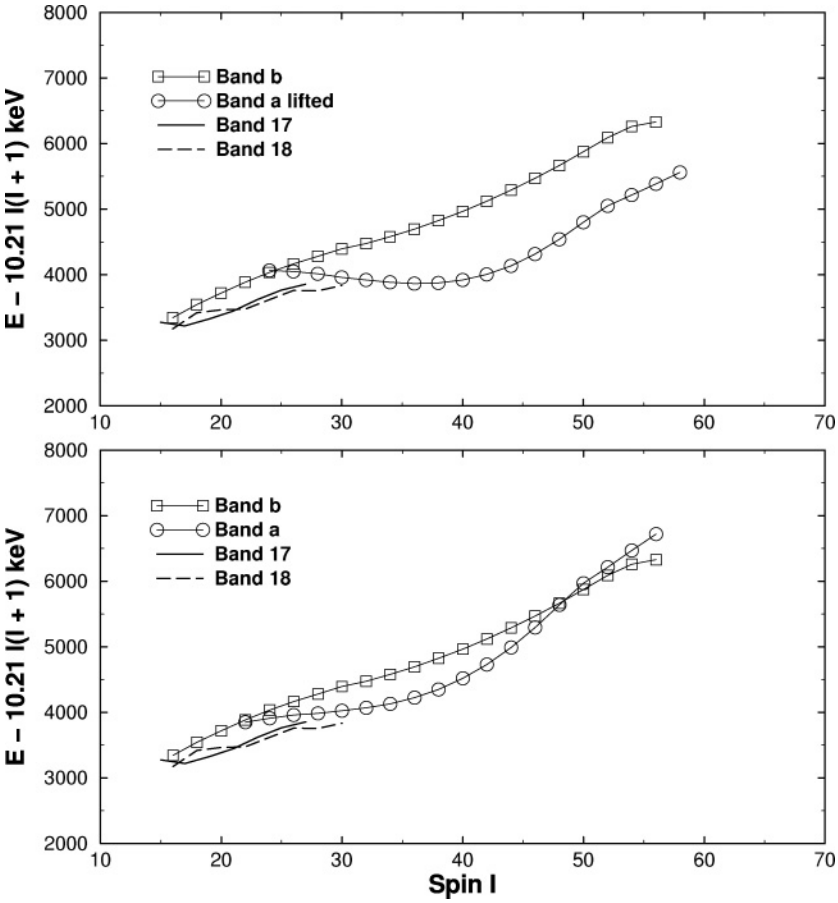

FIG. 6. Level energies of bands **a, b**, 17, and 18, with the energy of a rotating rigid core subtracted, are shown as a function of spin for two placements of band **a**. The lower panel shows band **a** for the adopted placement shown in Figs. 1 and 2, whereas the upper panel shows the band lifted by two units of spin and 1178 keV in energy.

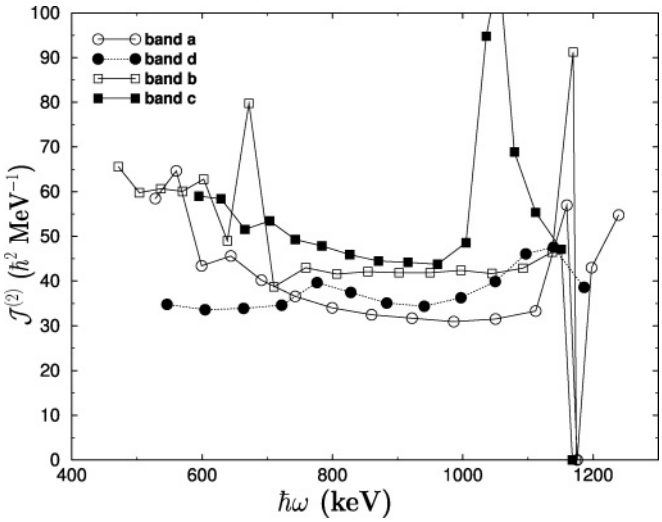

FIG. 7. Dynamic moments of inertia for the four long bands as a function of rotational frequency. Band crossings are seen at 1050 and at 1170 keV, whereas the spike at 675 keV is caused by an interaction between the 30^+ states in bands **b** and **b**+.

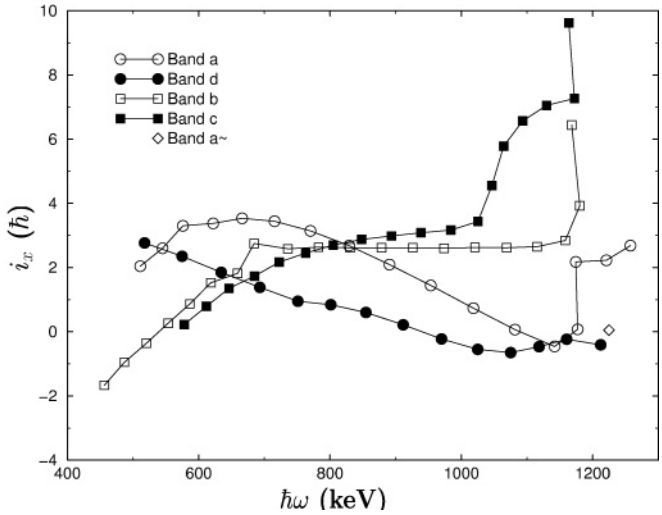

FIG. 8. Alignment of bands **a, b, c, d**, and **a** $\sim$ with Harris parameters $\mathcal{J}_0 = 42\hbar^2$/MeV and $\mathcal{J}_1 = 0$.

level energy lowers band **a** in the energy-spin plane and would result in a much stronger population relative to band **b** than the 10% difference we observe, see Sec. III C.

We find from Table II that band **a** receives 37 units of intensity in the spin range 32–44, whereas band **b** receives 35 units. This is, within uncertainties, in agreement with the 10% difference in population extracted by the multiple-gating technique described in Sec. III C. In the spin range of 48 to 54, however, the intensity ratio between bands **a** and **b** is inversed. Here the population intensity of band **b** is 5.6 units compared to 3.2 units for band **a**, which is in agreement with band **b** being closer to yrast than band **a** in this spin range. On the basis of these experimental intensities and the evolution of the two bands in the energy-spin plane, see Fig. 6, we conclude that the lower panel is the only one agreeing with the experiment and that the placement of band **a**, therefore, is most likely as proposed in Fig. 1. Accordingly, no parentheses on spin and parity are used for band **a**. Band **a** becomes yrast above $I \sim 30$, where bands 17 and 18 appear to terminate as regular rotational structures.

The dynamic moments of inertia $\mathcal{J}^{(2)}$, presented in Fig. 7, do not depend on assigned spin values, whereas the spin alignments, shown in Fig. 8, do. A lowering of $\sim$5 keV of the 25^- state of band **a**, which interacts with band **a** $\sim$ results in a smooth trend of the $\mathcal{J}^{(2)}$ for band **a** at $\hbar\omega \sim 580$ keV. Likewise the irregularity at $\hbar\omega \sim 700$ keV for band **b** is caused by its interaction with band $\mathbf{b}^+$ at $I = 30$, which can be removed by a shift of ~ -15 and $+15$ keV of the 30^+ levels of bands **b** and $\mathbf{b}^+$, respectively. Apart from these irregularities the dynamic moments of inertia show a grouping of the four long bands in pairs of **a**, **d** and **b**, **c**, which is consistent with the decay of the pair **a**, **d** to the lower-lying negative-parity structures and of the pair **b**, **c** to the positive-parity states. Another feature of the evolution of $\mathcal{J}^{(2)}$ is a relative constancy over a frequency range of about 500 keV. When comparing average values of $\mathcal{J}^{(2)}$ in the range $\hbar\omega \sim 750$–1100 keV, we observe a difference of $\sim 10\hbar^2$/MeV between the two pairs that might be interpreted as a difference in deformation, bands **b** and **c** being the more deformed ones. The average values of $\mathcal{J}^{(2)} = 35\hbar^2$/MeV and $45\hbar^2$/MeV, respectively, are far from the value of $56.4\hbar^2$/MeV, which is the calculated moment of inertia for a rigid prolate nucleus with an axis ratio of 1/1.3, corresponding to the value of Q_t determined for band **a** if assuming axial symmetry; see Sec. III D. This discrepancy might indicate that the system is not rigid, even at the highest spins observed in band **a**. However, as discussed below, the UC calculations reproduce both the quadrupole moment and the moments of inertia rather well. We note that the dynamic moments of inertia indicate crossings in all bands near $\hbar\omega = 1170$ keV and for band **c** another crossing at about 1050 keV.

The alignment of the long bands shows the simultanous crossing of bands **a**, **b**, and **c** at about 1170 keV, see Fig. 8. Band **d** does not indicate a crossing in this frequency region, but the trend of the alignment considering the last four transitions of this band could be explained by an unobserved forking transition, i.e., a lower branch with more alignment has not been observed. The dwindling intensity in band **d** at the highest spins and the observed forking of band **a** into **a** $\sim$ at $\hbar\omega \sim 1200$ keV support this suggestion. The additional crossing in band **c** at $\hbar\omega \sim 1050$ keV is clearly identified in Fig. 8.

The experimental determination of Q_t discussed in Sec. III D for band **a** compares well with a potential energy minimum obtained in the UC calculations [5] at $(\epsilon, \gamma) \sim (0.35, 5^\circ)$ and $\epsilon_4 \sim 0$. This minimum in the potential energy surface emerges at $I \sim 20$, becomes global and is stable over a long spin range, in particular for the lowest calculated quasiparticle configurations which correspond to the parity and signature combinations (π, α) possible for the four long bands. The agreement between the measured $Q_t = 5.2$ b (520 fm^2) and the values calculated within this minimum is clear from Fig. 9. [The UC code calculates the (static) electric quadrupole moment $\sqrt{\frac{8}{3}}\hat{Q}_2$ which within a regular rotational band with a stable shape, may be related to the measured transition quadrupole moment Q_t]. The further discussion of the four

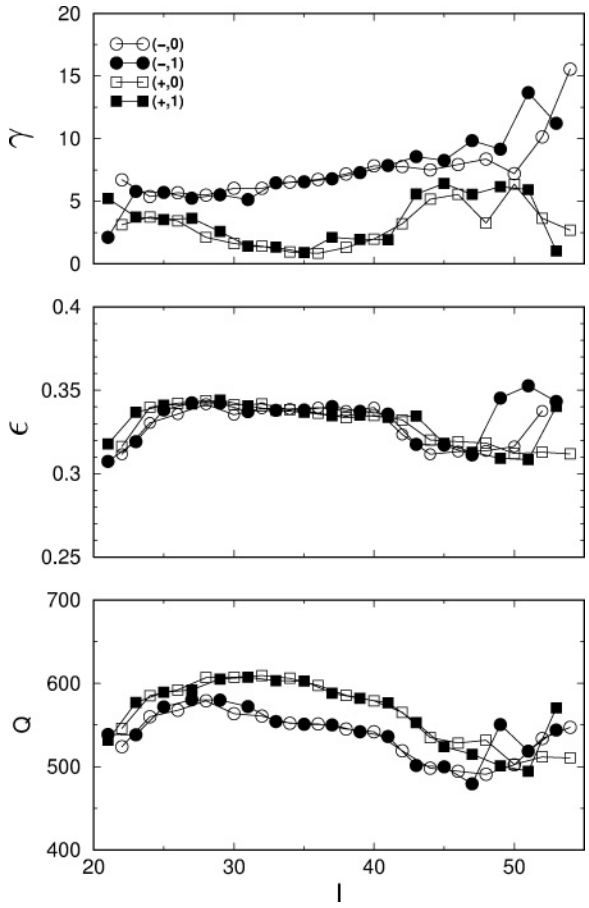

FIG. 9. Results of UC calculations for the quadrupole moment $Q = \sqrt{\frac{8}{3}}\hat{Q}_2$ in fm^2, the quadrupole deformation parameter ϵ and the gamma deformation in degrees, shown in the lower, middle, and upper panels, respectively vz spin. The stuctures with $(\pi, \alpha) = (-, 0)$, $(-,1)$, $(+,0)$, and $(+,1)$ we relate to the experimentally observed bands **a**, **d**, **b**, and **c**, respectively.

bands will, therefore, relate to the structural features at this minimum. We shall compare three of the features identified in Figs. 7 and 8 to results of UC calculations in some detail. One is the pairwise appearance of the four long bands, the other is the constancy of the $\mathcal{J}^{(2)}$ value over a frequency range of about 500 keV, and the third is the common upbend at a frequency of about 1170 keV.

The proton orbitals available close to the Fermi level are $g_{7/2}$ and $i_{13/2}$ with positive parity and $h_{11/2}$ with negative parity. For the neutrons, the $i_{13/2}$ orbitals with positive parity and the $h_{9/2}$, $h_{11/2}$ and $j_{15/2}$ orbitals with negative parity are available. We note that the latter neutron orbital as well as the $i_{13/2}$ proton orbital have large negative slopes of the energy as a function of frequency, $d(e)/d(\omega)$, and are, therefore, most probably active in the observed band crossings at high frequencies. The lowest structures with relevant spins and frequencies that have parity and signature $(-,0)$ and $(-,1)$ as bands **a** and **d** or $(+,0)$ and $(+,1)$ as bands **b** and **c**, have two to four quasiparticles excited in both the proton and the neutron systems. The lowest solutions involve $g_{7/2}$ and $h_{11/2}$ protons coupled to $i_{13/2}$ and $h_{11/2}$ neutrons, as shown in Table III.

TABLE III. Proton and neutron orbitals excited in bands with (π, α) corresponding to bands **a**, **b**, **c** and **d** below ∼0.7 MeV, according to calculations with the UC code.

Parity, signature (π, α)	protons orbitals, signature	neutrons orbitals, signature	Band exp.
$(-,0)$	$g^2_{7/2} \otimes h^2_{11/2}, 0$	$i_{13/2} \otimes h_{11/2}, 0$	**a**
$(-,1)$	$g^2_{7/2} \otimes h^2_{11/2}, 0$	$i_{13/2} \otimes h_{11/2}, 1$	**d**
$(+,0)$	$g_{7/2} \otimes h_{11/2}, 0$	$i_{13/2} \otimes h_{11/2}, 0$	**b**
$(+,1)$	$g_{7/2} \otimes h_{11/2}, 0$	$i_{13/2} \otimes h_{11/2}, 1$	**c**

An alternative structure for bands **b** and **c** is obtained by a simultaneous change of the signature quantum numbers of the occupied $h_{11/2}$ neutron and $g_{7/2}$ proton orbitals, which is not expected to change the band properties substantially. Both orbitals have no or a very small signature splitting in the relevant deformation and frequency region. The difference between the two pairs is, thus, to be traced to the excited quasiprotons, because the neutron excitations are pairwise identical. The positive-parity bands **b** and **c** have the $h^2_{11/2}$ alignment blocked, which may explain the difference in the alignment behavior of the two pairs of bands, which is also observed experimentally.

Structural changes resulting in an increase of the alignment might be expected for both pairs in at least two situations; first, at frequencies around 0.85–0.9 MeV where the $i_{13/2}$ proton competes with and crosses the $g_{7/2}$ proton with $\alpha = +1/2$ and, second, at frequencies around 1.2 MeV where the $j_{15/2}$ neutron competes with the $h_{11/2}$ neutron. Slowly increasing alignments are expected for the higher-frequency $i_{13/2}$ neutron crossing and are, therefore, not considered for causing the dramatic upbends experimentally observed in bands **a**, **b**, and **c**. We note that the location of the $i_{13/2}$ proton orbital is strongly dependent on deviations from axial symmetry of the nuclear shape and that this might argue against the first conjecture mentioned above. For the common alignment gain observed at $\hbar\omega \sim 1.17$ MeV we, therefore, suggest that the $j_{15/2}$ neutron has to be involved. For such multiquasiparticle bands it may be expected that pairing correlations are strongly reduced.

It is a striking feature of the UC calculations that our suggestion for bands **a** and **d** as signature partners with negative parity and bands **b** and **c** with positive parity is corroborated very nicely. Figure 9 shows the UC predictions for the quadrupole moment, the quadrupole deformation and the gamma deformation in the lower, middle, and top panels, respectively, as a function of spin. The pairwise features and the constancy of the calculated Q, ϵ, and γ deformations over an interval of about 30 units of spin in the range where the four bands are observed are characteristic for these calculated bands.

All three calculated quantities displayed in Fig. 9 start to deviate from their regular trends at about spin 45, a feature that has its basis in the relevant potential energy surfaces. The stable minimum at $\epsilon \sim 0.35$ gradually disappears for bands **a** and **d**, while it moves to larger γ values. The calculated values of Q_2 shown in Fig. 9 indicate a larger deformation for bands **b** and **c** than for the negative-parity pair. However,

this difference is entirely based on a difference in nonaxial symmetry that would barely be reflected in a larger moment of inertia. The UC code provides coordinates in the energy-spin plane which allow a comparison to experimental data in graphs (not shown) corresponding to Fig. 6. The calculated bands **a** and **b** are, in this representation, separated by ∼500 keV from $I \sim 30$ to 40, and they cross at $I \sim 48$ as in the experiment; see Fig. 6, lower panel. The signature partners, bands **d** and **c**, exhibit the same trend as bands **a** and **b**. For a more direct comparison with data, we have extracted the dynamic moment of inertia $\mathcal{J}^{(2)}$, equivalent to $d(I)/d(\omega)$, with the UC code for the two pairs. The pairwise splitting persists in a rotational frequency interval of about 400 keV and in the frequency region $\hbar\omega \sim 0.7$–0.95 MeV, the negative-parity pair has an average $\mathcal{J}^{(2)}$ of $\sim 35\hbar^2$/MeV, whereas the $\mathcal{J}^{(2)}$ of the positive-parity pair is $\sim 42\hbar^2$/MeV. The agreement with the experimental data in Fig. 7 is very satisfactory, for the positive-parity bands also with regard to the decreasing trend of the absolute values.

Figure 10 displays the experimental yrast levels together with a calculated yrast line, neutron separation energy, fission barrier and, at the highest spins, an yrast line expected for hyperdeformed (HD) states in ^{126}Xe, see figure caption for details. In neither of the spectra based on the Xe1 data set from Euroball nor the Xe2 data set from Gammasphere, do we find discrete transitions which link the bands shown in Figs. 1 and 2 directly to discrete band structures in a HD minimum. Figure 10 demonstrates that the gap in exitation energy and angular momentum between the top of bands **a** and **b** and the calculated HD yrast line is only about 3.5 MeV and ∼5 units of spin, respectively, corresponding to two to three transitions of $E2$ character. However, a filtering of high-fold

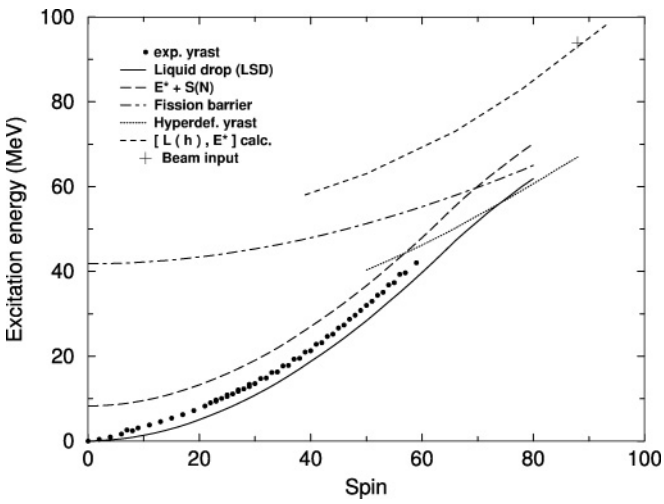

FIG. 10. Yrast diagram for ^{126}Xe. The experimentally measured yrast level energies are plotted as filled dots. The calculated yrast line based on the LSD model [4] is shown as a solid line. The long dashed curve shows the sum of the calculated yrast energy and the neutron separation energy $S(N)$. The fission barrier [4] is shown as a dashed-dot line. The yrast line corresponding to a hyperdeformed band with a moment of inertia $100\hbar^2$/MeV is drawn with small dots. The calculated maximum angular momentum and excitation energy input from the reaction is indicated by a plus sign.

events [18] with the characteristics of bands **a**, **b**, **c**, and **d** reveals a ridge structure in the unresolved quasicontinuum spectra with a distance between the ridges corresponding to an energy difference between consecutive rotational transitions of $\triangle E_\gamma \sim 48$ keV. The energy difference relates to the moment of inertia as

$$\triangle E_\gamma = \frac{4\hbar^2}{\mathcal{J}^{(2)}}$$

and corresponds to a value of $\mathcal{J}^{(2)} = 83\hbar^2$/MeV. Such a large moment of inertia is evidence for a strongly deformed rotor. However, it is smaller than the $\sim 100\hbar^2$/MeV expected for hyperdeformation in ^{126}Xe and rather suggests that the ridges originate from superdeformed states [19]. A detailed analysis of the ridges by a fluctuation technique [20] reveals that they represent about 10 bands with a γ-ray multiplicity in the range from 18 to 26.

V. CONCLUSIONS

The nucleus ^{126}Xe has been populated to very high spins in two experiments where the most powerful Ge-detector arrays worldwide, Euroball and Gammasphere, have been used. Calculated values for the angular momentum inputs, taking target deformations into account, gives a maximum of $90\hbar$. This should be sufficient to populate HD structures and to study their decay toward the ground state. In spite of a number of ancillary detectors, high statistical accuracy and good energy resolution of the Ge-detector arrays, no discrete-line spectra originating from rotating HD nuclei could be identified.

Instead, the results have provided new, detailed structure information in an energy range up to about 42 MeV of excitation and 59 units of spin in ^{126}Xe. The most striking feature of these structures is the presence of four regular bands which span a spin range of almost $40\hbar$. The structure of these bands has been compared to cranked shell-model calculations with the UC code [5] and good correspondence between experiment and theory has been demonstrated. An analysis of peak widths of the transitions in the strongest populated band for an estimate of recoil velocities as a function of the transition energy has given a value for the transition quadrupole moment, which agrees well with the one calculated by the UC code for states in a deformed potential-energy minimum. The properties of four of the calculated band structures reproduce parities, signatures, moments of inertia, and crossing frequencies of the four experimentally observed bands very well. The band structures extend to within about two to three transitions from a crossing with the predicted HD yrast line. A ridge analysis of the unresolved quasicontinuum spectra from the present set of data indicates that the four long bands are preceeded by quasicontinuum bands located in a superdeformed minimum.

ACKNOWLEDGMENTS

The authors thank the staff of the former IReS institute for the operation of the VIVITRON and the Euroball array under contract EUROVIV HPRI-CT-1999-00078. The authors also thank the ANL operations staff at Gammasphere and are

indebted to J. P. Greene for his help in target preparation. G. Sletten is grateful to the GANIL management for providing excellent working conditions during the writing phase of this work. This research was supported by the Danish FNU council for the natural sciences, by the German BMBF under contract 06 BN 109, by the Polish Ministery of Science and Higher Education under grant P03B 030 30, and by the U.S. Department of Energy, Office of Nuclear Physics under contracts DE-AC02-06CH11357 (ANL) and DE-AC03-76SF00098 (LBNL).

[1] A. Granderath, P. F. Mantica, R. Bengtsson, R. Wyss, P. von Brentano, A. Gelberg, and F. Seiffert, Nucl. Phys. **A597**, 427 (1996).
[2] F. Seiffert, W. Lieberz, A. Dewald, S. Freund, A. Gelberg, A. Granderath, D. Lieberz, R. Wirowski, and P. von Brentano, Nucl. Phys. **A554**, 287 (1993).
[3] S. Cohen, F. Plasil, and W. J. Swiatecki, Ann. Phys. **82**(2), 557 (1974).
[4] K. Pomorski and J. Dudek, Phys. Rev. C **67**, 044316 (2003); N. Schunck, J. Dudek, and B. Herskind, Phys. Scr. T **125**, 218 (2006); N. Schunck, J. Dudek, and B. Herskind, Phys. Rev. C **75**, 054304 (2007).
[5] R. Bengtsson, Nucl. Phys. A **512**, 124 (1990).
[6] B. Herskind, G. Benzoni, J. N. Wilson, T. Dossing, G. B. Hagemann, G. Sletten, C. Ronn Hansen, D. R. Jensen, A. Bracco, F. Camera, S. Leoni, P. Mason, O. Wieland, A. Maj, M. Brekiesz, M. Kmiecik, H. Huebel, P. Bringel, A. Neusser, A. K. Singh, R. M. Diamond, R. K. Clark, M. Cromaz, P. Fallon, A. Goergen, I. Y. Lee, A. O. Macchiavelli, D. Ward, F. Hannachi, A. Korichi, A. Lopez-Martens, T. Byrski, D. Curien, P. Bendnacrzyk, J. Dudek, H. Amro, W. C. Ma, J. Lisle, S. Odegård, C. Petrache, D. Petrache, T. Steinhardt, O. Thelen, Acta. Phys. Pol. B **34**, 2467 (2003).
[7] H. Hübel, Acta Phys. Pol. B **36**, 1015 (2005).
[8] B. M. Nyakó, J. R. Cresswell, P. D. Forsyth, D. Howe, P. J. Nolan, M. A. Riley, J. F. Sharpey-Schafer, J. Simpson, N. J. Ward, and P. J. Twin, Phys. Rev. Lett. **52**, 507 (1984).
[9] P. J. Twin, B. M. Nyakó, A. H. Nelson, J. Simpson, M. A. Bentley, H. W. Cranmer-Gordon, P. D. Forsyth, D. Howe, A. R. Mokhtar, J. D. Morrison, J. F. Sharpey-Schafer, and G. Sletten, Phys. Rev. Lett. **57**, 811 (1986).
[10] J. Simpson, Z. Phys. A **358**, 139 (1997).
[11] http://www-gam.lbl.gov.
[12] J. P. Green, AIP Conf. Proc. **475**, 929 (1999).
[13] D. C. Radford, Nucl. Instrum. Methods A **361**, 297 (1995).
[14] A. Neußer, H. Hübel, A. Al-Khatib, P. Bringel, A. Bürger, N. Nenoff, G. Schönwaßer *et al*., Phys. Rev. C **70**, 064315 (2004).
[15] B. Cederwall, I. Y. Lee, S. Asztalos, M. J. Brinkman, J. A. Becker, R. M. Clark, M. A. Deleplanque, R. M. Diamond, P. Fallon, L. P. Farris, E. A. Henry, J. R. Hughes, A. O. Macchiavelli, and F. S. Stephens, Nucl. Instrum. Methods A **354**, 591 (1995).
[16] J. F. Ziegler, J. P. Biersack, and U. Littmark, in *The Stopping Power and Range of Ions in Matter* (Pergamon, New York, 1985), Vol. 1.
[17] A. Görgen, G. B. Hagemann, I. Hamamoto, R. Bengtsson, R. M. Clark, M. Cromaz, P. Fallon, H. Hübel, I. Y. Lee, A. O. Macchiavelli, G. Sletten, and D. Ward, AIP Conf. Proc. **764**, 9 (2005).
[18] J. N. Wilson and B. Herskind, Nucl. Instrum. Methods A **455**, 612 (2000).
[19] B. Herskind, G. B. Hagemann, G. Sletten, T. Døssing, C. Rønn Hansen, N. Schunck, S. Ødegaard, H. Hübel, P. Bringel *et al*., Physica Scripta T **125**, 108 (2006).
[20] T. Døssing, B. Herskind, S. Leoni, A. Bracco, R. A. Broglia, M. Matsuo, and E. Vigezzi, Phys. Rep. **268**, 1 (1996).